



Nonlinear Dependence of Photocarrier Radiometry Signals from p-Si Wafers on Optical Excitation Intensity

Jordan Tolev,^a Andreas Mandelis,^{a,z} and Michal Pawlak^{a,b,c}

^aDepartment of Mechanical and Industrial Engineering, Center for Advanced Diffusion-Wave Technologies, University of Toronto, Toronto, Ontario M5S 3G8, Canada

^bExperimental Physics III, Ruhr-Universität Bochum, Germany

^cInstitute of Physics, Nicolaus Copernicus University, Torun, Poland

The dependence of the photocarrier radiometric (PCR) signal on the intensity of exciting superbandgap laser radiation was investigated. It was shown that the amplitude of the PCR signal exhibits a supralinear dependence on laser intensity I_0^β , with nonlinearity coefficient/exponent β such that $1 \leq \beta \leq 2$. The power dependence of the amplitude is an important indicator of the photoexcited carrier recombination physics in semiconductors ranging between monopolar ($\beta = 1$) and bipolar ($\beta = 2$) limits. The study was made with laser beams of varying wavelength, power, and spotsize and with semiconductor silicon wafers with different transport parameters, especially recombination lifetime. One-dimensional and three-dimensional models of the nonlinear PCR signal dependence on β vs modulation frequency were developed. It was found that the conventional linear approach using $\beta = 1$ is not always consistent with experimental slopes of amplitude vs power and it may yield erroneous values of the electronic transport properties. Consideration of the fundamental and second harmonic amplitudes and phases of the PCR signal showed that the physical origin of the nonlinear dependence of the PCR amplitude on laser intensity is consistent with high-optical-injection of free-carriers in the semiconductor. The value of β can also be determined by the second harmonic-to-fundamental-amplitude ratio and is controlled by the carrier relaxation time dependence on the optically injected excess diffusive photocarrier density wave.

© 2007 The Electrochemical Society. [DOI: 10.1149/1.2780862] All rights reserved.

Manuscript submitted March 26, 2007; revised manuscript received June 25, 2007. Available electronically September 21, 2007.

Among the physical parameters of semiconductors, the electronic transport properties, namely, carrier recombination lifetime τ , carrier diffusion coefficient D , and front- and rear-surface recombination velocity S_1 and S_2 , have attracted great attention in semiconductor device manufacturing. Evaluation of these parameters is essential for characterizing semiconductor wafers, for defect and contamination monitoring, and for device modeling.¹ The technique of laser-induced infrared photocarrier radiometry (PCR) is an optoelectronic carrier density-wave diagnostic method for noncontact characterization of the electronic transport properties of semiconductors. This technique is a form of quantitative dynamic photoluminescence; it relies on the detection of modulated diffuse radiative emissions from semiconductors obeying Kirchhoff's law under conditions of near-thermodynamic equilibrium of an electronic solid when the latter is optically excited by intensity-modulated laser radiation with photon energy greater than the fundamental energy gap of the material. To determine the transport properties, both amplitude and phase of the PCR signal are simultaneously recorded as functions of angular modulation frequency ($\omega = 2\pi f$) over several orders of magnitude and then fitted to suitable theoretical models [either one dimensional (1D) or three dimensional (3D)] via a multiparameter fitting procedure.^{2,3} To date, PCR has been developed as a linear technique, in the sense that the amplitude of the signal depends linearly on laser power at low power ranges. PCR signal nonlinearities associated with the existence of a space-charge layer in silicon and the effects of optical biasing and conditioning of this layer in the flatband configuration under low-intensity conditions have also been observed by our group.⁴

Guidotti et al.⁵ did explore theoretically and experimentally the laser power dependence of modulated photoluminescence (PL) in 10–15 Ω cm p-Si corresponding to equilibrium hole density $p_0 = 1 \times 10^{15}$ cm⁻³ under room-temperature conditions. They found a sharp linear-to-quadratic transition using a 647 nm krypton–argon laser with the quadratic threshold at incident power ~ 5 mW corresponding to an excess electron-hole density $\sim 3 \times 10^{16}$ cm⁻³. They attributed the linear range to recombination of photoexcited carriers via donor (or acceptor) density of states present primarily due to semiconductor doping. Recombination in the presence of impurities and dopants in Si has been known to be a source of room-

temperature PL since the 1950s.⁶ The quadratic behavior was explained as being due to bipolar recombination via photogenerated electron and hole densities of states. A superposition of linear and quadratic dependence on laser intensity of spectrally integrated dc PL emission in layered semiconductors (InP/InGaAs/InP) has been reported by Nuban et al.^{7,8} Given the effective recombination lifetime τ

$$\frac{1}{\tau} = \frac{1}{\tau_R} + \frac{1}{\tau_{NR}} \quad [1]$$

where τ_R and τ_{NR} are the radiative and nonradiative lifetime, respectively; the integrated PL can be expressed as $PL(I_0) = CB_R\tau(NI_0 + 1/2\sqrt{(\tau/D)I_0^2})$, where I_0 is the excitation intensity, B_R is the radiative recombination coefficient, D is the photocarrier diffusion coefficient, N is the free-carrier concentration, and C is a proportionality constant. The linear regime is attained when $\tau \approx \tau_R \ll \tau_{NR}$ when all carriers recombine radiatively and its efficiency is a function of lifetime and doping density. The quadratic limit is attained at high excitation levels where PL depends largely on electron-hole recombination lifetime. In those studies it was assumed that the effective lifetime, τ , is independent of the excess carrier density. This assumption, however, is only valid under very restrictive conditions of injection level.⁹ Reinhart¹⁰ has studied the excitation power and intensity dependence of dc PL in undoped semiconductors due to nonlinear recombination and diffusion, primarily the quadratic and cubic dependencies of the radiative and Auger recombination rates on the excess photocarrier density N . He pointed out that the concept of universal recombination lifetime is not valid in intrinsic and lightly doped semiconductors. Although materials, physical processes, and PCR signal generation and detection are quite different from Ref. 10, in the present study we have verified that recombination lifetime strongly depends on laser power/intensity. In the course of experimenting with PCR signal amplitude dependencies of Si wafers on laser intensity, expecting a linear-to-quadratic transition, we observed that there is no such clear-cut dependence but rather a supralinear dependence on laser intensity, I_0^β , with nonlinearity coefficient/exponent β such that $1 \leq \beta \leq 2$.

In this study, the nonlinear dependence of the amplitude and the phase of the PCR signal on the power/intensity of the modulated incident superbandgap laser parameters (wavelength and spotsize) is theoretically developed and experimentally obtained for long and

^z E-mail: mandelis@mie.utoronto.ca

short recombination-lifetime Si wafers. The physical origins of the nonlinearity coefficient β , the slope of the PCR amplitude dependence on laser power/intensity, are studied in terms of the dependence of the free-carrier absorption coefficient on the relaxation time, τ_S , of free photoexcited carriers contributing to sub-bandgap (near-infrared) absorption by the diffusive free-carrier density wave under harmonically modulated laser excitation. The nonlinear theory is applied to the extraction of the transport parameters of the semiconductor by means of multiparameter best fits in models in one and three dimensions, depending on the ratio of spotsize of the excitation laser beam to sample thickness and/or carrier diffusion length. The measurements have allowed the estimation of the error committed when performing theoretical best fits to the PCR amplitude and phase data using the conventional linear PRC theory² without regard to the nonlinearity coefficient.

PCR Nonlinear Theoretical Models

When a semiconductor is illuminated with superbandgap light of photon energy $h\nu$, electrons in the valence band absorb the incident energy and cross the forbidden energy gap toward the conduction band, leaving an equal number of holes in the valence band. The excess electrons and holes become thermalized with the lattice through phonon interactions on a short time scale, releasing the excess energy $h\nu - E_g$, where E_g is the bandgap of the semiconductor. Then, the photogenerated excess electrons and holes diffuse for a short time, known as effective carrier lifetime τ , Eq. 1, before they recombine through nonradiative or radiative recombination processes, giving off thermal energy to the lattice and/or emitting PL photon flux, usually in the form of near-infrared diffuse radiation known as Kirchhoff's law when the quantum states of the medium obey the equilibrium distribution regardless of the temperature distribution of the radiation field (Weinstein–Bauer conditions).^{2,11} Quantitative formulation of the time-dependent Weinstein–Bauer problem of nonequilibrium excess-carrier-density recombination and radiative emission and transfer under near-equilibrium (Kirchhoff-law governed) conditions and its experimental implementation for time-harmonic optical excitation led to the emergence of PCR.² In PCR measurements of silicon, a modulated laser beam is used for carrier photoexcitation and the midinfrared thermal (Planck-mediated) emissions are filtered out. An appropriate near-infrared (NIR) detector and spectrally matched filter combination detects only NIR emissions from the free photogenerated carrier-wave component. The optically injected three-dimensional excess carrier density N is calculated from the following carrier transport equation

$$\nabla^2 N(r, z, \omega) - \sigma_n^2 N(r, z, \omega) = -\frac{G(r, z, \omega)}{D_n} \quad [2]$$

where D_n the carrier diffusivity of the semiconductor and

$$\sigma_n = \sqrt{\frac{1 + i\omega\tau}{D_n\tau}} \quad [3]$$

is the n-type carrier wavenumber. The source term in Eq. 2 is given by

$$G(r, z, \omega) = \frac{\alpha_p \eta_n P_0 (1 - R)}{2h\nu\pi W^2} \exp\left(-\frac{r^2}{W^2} - \alpha_p z\right) \exp(i\omega t) \quad [4]$$

Here P_0 is the power of the incident laser, R is the surface reflectivity of the sample, α_p is the semiconductor absorption coefficient at the pump beam wavelength, η_n is the optical-to-electronic energy conversion efficiency, and W is the laser-beam spotsize (defined as the e^{-2} point of the Gaussian distribution of the laser beam). The corresponding intensity on the surface of the semiconductor is $I_0 = P_0/\pi W^2$. In the relaxation-time approximation in semiconductors, the energy-dependent relaxation time tensor, τ_S , has the same principal axes as the effective-mass tensor, m^* , with principal values τ_{\parallel} and τ_{\perp} , where the subscripts indicate directions parallel and perpendicular to the ellipsoidal constant energy surfaces. In the semiclassical theory of free-carrier contribution to the dielectric function of

semiconductors, the Drude–Zener approximation is obtained for isotropic τ_S , when the carrier density is degenerate. In that limit τ_S reduces to a scalar relaxation time, τ_S ,¹² with magnitude on the order of 1×10^{-14} s for n-Si.¹³ In n-Si this occurs at free-carrier densities $N \geq 10^{20}$ cm⁻³. The result is the Drude equation for free-carrier absorption coefficient α_f in n-type Si with hole density $p \ll n$

$$\alpha_f(N) = \frac{Nq^2\lambda^2}{8\pi^2nc^3m^*\tau_S(N)} \quad [5]$$

where N is the electron concentration, m^* is the isotropic electron effective mass, n is the refractive index, and c is the speed of light in the semiconductor. A similar expression is valid for p-type semiconductors provided that N is replaced by P , the free hole density.

Considering a system of a homogeneous semiconductor wafer polished on one side and a superbandgap laser beam of spotsize W focused on the same side, the PCR signal depends on the density of the photogenerated excess diffusive carrier-wave $N(r, z, \omega)$. In one dimension it can be expressed by the equation²

$$S_{1-D}(\omega) \approx F(\lambda_1, \lambda_2) \int_0^L \alpha_f[N(z, \omega; \lambda)] dz \quad [6]$$

where $F(\lambda_1, \lambda_2)$ is a function of the surface reflectivity of the semiconductor, its radiative quantum efficiency, and the spectral power per unit wavelength (the product of recombination transition rate from band to band, or from bandedge to defect or impurity state, as the case may be, and the energy difference between initial and final states). L is the thickness of the semiconductor and λ_1, λ_2 , are the limits of the spectral bandwidth of the IR detector, $\lambda_1 \leq \lambda \leq \lambda_2$. If there is no N -dependence of the relaxation time τ_S in Eq. 5, the 3D extension of Eq. 6 is straightforward, taking into account Eq. 5, and can be expressed by the equation¹⁴

$$S_{3D}(\omega) = \frac{C_{3D}}{\pi A} \int_0^\infty \Delta\tilde{N}(q; \omega) J_1(qA) dq \quad [7]$$

which is linear in the excess carrier-wave density. Here C_{3D} is a proportionality coefficient depending on the spectral range of the photodetector; $J_1(X)$ is the Bessel function of the first kind of order 1; A is the effective detector radius; $\Delta\tilde{N}(q, \omega)$ is the depth integral of the Hankel transform, $\tilde{N}(q, z, \omega)$, of the carrier-density-wave field, obtained as a solution of the carrier transport equation, Eq. 2

$$\Delta\tilde{N}(q; \omega) = \int_0^L \tilde{N}(q, z; \omega) dz = E_{3D}(q, \omega) M_{3D}(q, \omega) \quad [8]$$

where $M_{3D}(q, \omega)$ and $E_{3D}(q, \omega)$ are 3D semiconductor transport parameter-dependent terms described in Appendix A.

In cases where the frequency-dependent carrier diffusion length¹⁵ is much shorter than the spotsize of the focused superbandgap laser beam, the 1D limit of the excess carrier-density wave, Eq. 2, is obtained. Then, the PCR signal can be expressed as

$$S_{1D}(\omega) = C_{1D} \int_0^L N(z; \omega) dz = C_{1D} E_{1D}(\omega) M_{1D}(\omega) \quad [9]$$

Here C_{1D} is a coefficient which depends on the spectral bandwidth of the photodetector, $M_{1D}(q, \omega)$ is the 1D carrier-wave expression given in Appendix B, Eq. B-3. It describes the semiconductor transport parameter-dependent term. $E_{1D}(q, \omega)$ is described by Eq. B-2. Phenomenologically, the amplitude of the PCR signal $|S_{PCR}(\omega)|$ is a nominally linear function of the incident laser power P_0 , or intensity I_0 , but, in view of the N -dependence of the Drude Eq. 5, it can be generalized as

$$|S_{PCR}(\omega)| = aP_0^\beta = bI_0^\beta \quad [10]$$

where the experimental value of β is given by the slope

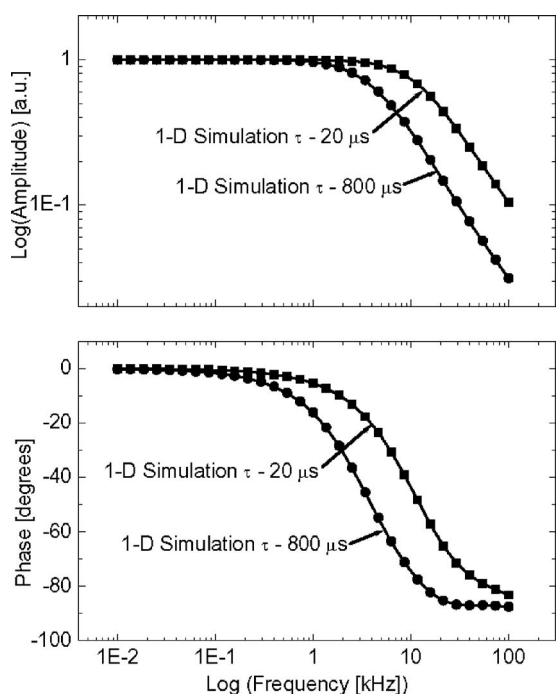


Figure 1. PCR frequency scan simulations with short and long carrier recombination lifetimes using 1D and 3D theoretical model with $\beta = 1$. 3D simulations with $\tau = 20$ (■) and $800 \mu\text{s}$ (●); 1D simulations with $\tau = 20$ (—) and $800 \mu\text{s}$ (—) coincide with the corresponding 3D simulation. Other transport parameters: $D = 15 \text{ cm}^2/\text{s}$, $S_1 = 200 \text{ cm/s}$, $S_2 = 10^5 \text{ cm/s}$, $\alpha_p = 659 \text{ cm}^{-1}$. Laser beam spotsize: 4 mm . $\beta = 1$

$$\beta = \frac{\Delta \ln |S_{\text{PCR}}(\omega)|}{\Delta \ln(P_0)} \quad [11]$$

Here a and b are constants, and β is the nonlinearity coefficient/exponent. The solution to Eq. 2 or its 1D version yields the excess free-carrier density-wave linear dependence on $I_0: N(r, z, \omega) = I_0 F(r, z, \omega)$. However, in general, the electron relaxation time $\tau_S(N) = CN^{-\gamma}$, $0 < \gamma < 1$; for instance, at near-degenerate densities of the order of 10^{18} cm^{-3} and higher, it has been found that $\gamma = 1/2$ for Ge.¹⁶ In this range of densities electronic transport is limited by impurity or carrier-carrier scattering. Therefore, $\beta = 1 + \gamma$ and $\alpha_f(N) \propto I_0^{1+\gamma}$. The 1D and 3D PCR signals in Eq. 6 and 7 respectively, become $S_{1D}(I_0) \sim I_0^{1+\gamma}$; $S_{3D}(I_0) \sim I_0^{1+\gamma} \sim P_0^{1+\gamma}$. The 3D Eq. 8 can be generalized using Eq. A-2 and A-3

$$\Delta \tilde{N}^\beta(q; \omega) = \int_0^L \tilde{N}^\beta(q, z; \omega) dz = \frac{\alpha_p I_0 \eta_n (1-R) e^{-q^2 W^2/4}}{2h\nu D [\alpha_p^2 - \xi_c^2]^\beta} M_{3D}^\beta(q, \omega) \quad [12]$$

whereas the 1D Eq. 9 with Eq. B-2 and B-3 and becomes

$$\Delta N^\beta(\omega) = \int_0^L \Delta N^\beta(z; \omega) dz = \frac{\alpha_p I_0 \eta_n (1-R)}{2h\nu D [\alpha_p^2 - \sigma_c^2]^\beta} M_{1D}^\beta(\omega) \quad [13]$$

Finally, the corresponding nonlinear PCR signal equations can be written as generalizations of Eq. 9 and 7

$$S_{1D}(\omega; \beta) = C_{1D} E_{1D}^\beta(\omega) M_{1D}^\beta(\omega) \quad [14]$$

and

$$S_{3D}(\omega; \beta) = \frac{C_{3D}}{\pi A} \int_0^\infty E_{3D}^\beta(q; \omega) M_{3D}^\beta(q; \omega) J_1(qA) dq \quad [15]$$

Figure 1 shows frequency-scan simulations in two sets of linear

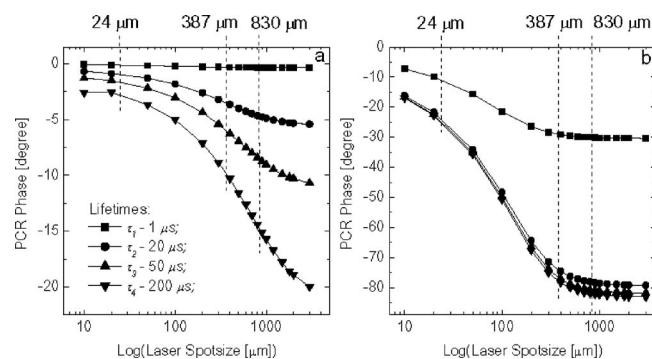


Figure 2. 3D simulation of laser beam spotsize dependence of PCR phases for frequency (a) 1 and (b) 100 kHz with a broad range of lifetimes and otherwise equal transport parameters: $D = 10 \text{ cm}^2/\text{s}$, $S_1 = 500 \text{ cm/s}$, $S_2 = 10^5 \text{ cm/s}$, $\alpha_p = 659 \text{ cm}^{-1}$.

PCR signals ($\beta = 1$) from silicon based on 1D and 3D theoretical models (Eq. 6 and 7, respectively) with laser wavelength 830 nm , spotsize 4 mm , and recombination lifetimes $\tau = 20$ and $800 \mu\text{s}$. The optical absorption coefficient was taken to be $\alpha_p = 635 \text{ cm}^{-1}$.¹⁷ The carrier transport parameters were assumed equal for both sets of curves. The amplitude curves are normalized to unity at $f = 10 \text{ Hz}$. It is clear that the simulations using the 1D and 3D equations coincide, as expected, for the chosen large spotsizes compared to the maximum carrier-wave diffusion length, $L_D(\omega) = |\sigma_n(\omega)|^{-1}$ at the lowest frequency $f = 10 \text{ Hz}$, where $L_D(10 \text{ Hz}) = 173.2 \mu\text{m}$ for $\tau = 20 \mu\text{s}$ and $1095 \mu\text{m}$ for $\tau = 800 \mu\text{s}$. In practice, the use of 1D theory to explain PCR data is warranted when changing laser beam spotsize on the semiconductor surface does not produce measurable change in 3D theory simulated PCR phase. This is an important dimensionality criterion; therefore, the dependence of the PCR phase on laser spotsize using the 3D theory with various lifetimes (or diffusion lengths of the photoexcited free carrier density wave) at two frequencies is presented in Fig. 2. On top of each figure three experimental spotsizes are highlighted. It is clearly seen that for PCR signals with $\tau = 1 \mu\text{s}$, 1D theory can be valid with spotsizes $2 \text{ W} \geq 387 \mu\text{m}$ at 1 and 100 kHz. However, with $\tau = 20, 50,$ and $200 \mu\text{s}$, the condition $2 \text{ W} \geq 830 \mu\text{m}$ is required at 100 kHz. In the latter cases all lower frequency ranges require a 3D theoretical approach.

Materials and PCR Instrumentation

In our experiments the superbandgap laser intensity and frequency dependence of PCR signals were studied using a setup with 532 nm wavelength and $18 \mu\text{m}$ spotsize and another setup with 830 nm wavelength and $24, 387,$ and $830 \mu\text{m}$ spotsizes. Best fits to experimental amplitude and phase data of the 1D and 3D linear and supralinear theoretical models were made with computational algorithms developed for this purpose and based on Eq. 14 and 15. Due to the double integration (over depth z and Hankel variable q) in inverting Eq. 15 to the spatial domain for arbitrary noninteger values of the nonlinearity exponent β , we were only able to use the 3D model with $\beta = 1$ and 2. The nonlinear 1D model, Eq. 14, involves only one integration over z ; therefore, it could be used with all values of $\beta \in [1, 2]$.

Experiments were performed with two (100) p-type (boron-doped) Si wafers. One wafer with a relatively long lifetime, 6 in. diameter, thickness $675 \pm 20 \mu\text{m}$, and resistivity $14\text{--}24 \Omega \text{ cm}$, was labeled M28. The other wafer, with a relatively short lifetime, 4 in. diameter, thickness $525 \pm 20 \mu\text{m}$, resistivity $20\text{--}25 \Omega \text{ cm}$, was labeled B501. Both wafers had a 500 \AA thermal oxide layer and were placed on a mirror sample holder to amplify the PCR signals.²

830 nm PCR system.— The 830 nm setup is shown in Fig. 3. Radiation from a laser diode (model Melles-Griot 561CS115) was

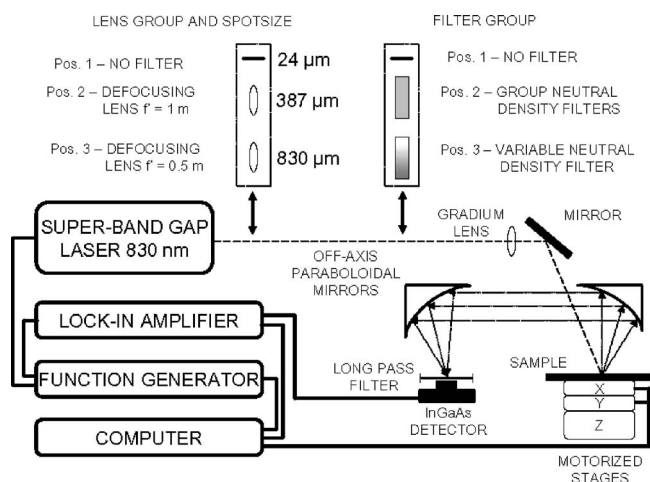


Figure 3. Experimental system for PCR measurements with superbandgap laser wavelength 830 nm.

harmonically modulated using a function generator (SRS model DG535) and was focused by a Gradium lens (focal length 125 mm) to a spot of 24 μm diameter on the polished wafer surface. The diameter of the focused laser beam could be changed to 387 and 830 μm by introducing a defocusing lens. With a variable neutral-density filter, the laser power was gradually varied from 1.8 to 15.6 mW and from 13.6 to 37.5 mW for the long and short recombination lifetime wafers, respectively. In this manner PCR signals vs laser intensity were obtained. Furthermore, using fixed optical-density-neutral filters, the frequency dependence of the PCR signals from wafer M28 was investigated with incident power 9.6, 15.2, and 20 mW. Similar frequency scans with wafer B501 were performed using 12 and 38 mW. The PCR NIR emissions from the wafers were collimated and collected by two off-axis paraboloidal mirrors and were detected using an InGaAs detector (ThorLabs model DET410). The spectral response of this photodetector is in the range 700–1800 nm and its frequency bandwidth is dc–10 MHz. The output signal was fed to a lock-in amplifier (EG&G model 5210) and the demodulated amplitudes and phases were processed by a personal computer.

532 nm PCR system.—This is a highly focused PCR microscopy system, shown in Fig. 4. Radiation from a Coherent model Verdi V10 diode-pumped laser was harmonically modulated by an acousto-optic modulator (AOM) (ISOMET model 1205C-2). The modulated beam was directly focused by a Gradium lens (focal

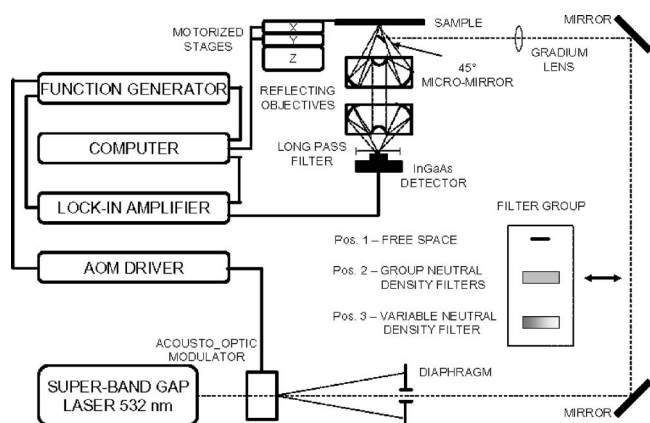


Figure 4. Experimental system for PCR measurements with superbandgap laser wavelength 532 nm.

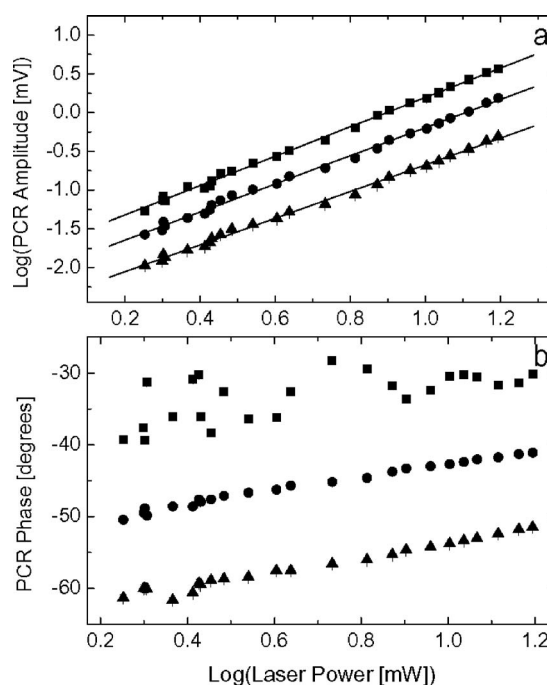


Figure 5. (a) Log-log plot of PCR amplitude and (b) lin-log plot of phase vs laser power at 830 nm and 10 kHz from wafer M 28 and 24 (■), 387 (●), and 830 μm (▲) spot sizes of the focused laser beam. Slopes of the corresponding best fits (—) for amplitudes: $\beta = 1.90$ (24 μm); 1.82 (387 μm); 1.72 (830 μm).

length 60 mm) to the polished surface of the wafers following a 90° reflection from a 45° micromirror attached to the collecting reflecting objective (Ealing/Coherent model 25-0522). The beam spot size was 18 μm. Under the high-intensity conditions of this experimental configuration, a signal stabilization period was necessary, during which the PCR amplitude reached a constant level while the phase remained constant, before any measurements were recorded. In order to avoid unnecessary exposure of the samples to laser irradiation leading to PL fatigue, the beam was interrupted between successive measurements. The PCR NIR emissions from the samples were collected and collimated by the silver-coated reflecting objective and focused onto an InGaAs detector (Thorlabs model DET410) with a second reflecting objective (Ealing/Coherent model 25-0506). The output signal was fed to a lock-in amplifier (model SRS 850 DSP) and processed by a personal computer. All frequency-dependent measurements made on both setups were normalized by the corresponding wide-bandwidth instrumental transfer functions. The transfer functions were obtained by measuring the amplitude and phase of modulated laser radiation (830 or 532 nm), scattered from a microscopically rough metallic surface positioned at the focal plane of the parabolic mirror, and partly transmitted through the filter.

Results and Discussion

Laser power dependencies.—The first group of experiments explored the laser power dependence, P_0 of the amplitude and phase of the PCR signal. In the context of our nonlinear experiments it is often necessary to refer to power and laser spot size separately instead of lumping them into an intensity figure. This occurs when the dimensionality of signals becomes a factor affecting theoretical interpretation and transport parameter extraction. Figure 5 shows results from wafer M28 made on the 830 nm setup shown in Fig. 3 at 10 kHz. Laser power dependencies of the PCR signal were obtained and slopes in log-log plots of amplitudes (Fig. 5a) vs power were calculated. The laser power was varied in the range 1.8–5.6 mW. Slopes β were calculated from Eq. 11 and were found to be 1.90, 1.82, and 1.72 for spot sizes 24, 387, and 830 μm, respectively. It is

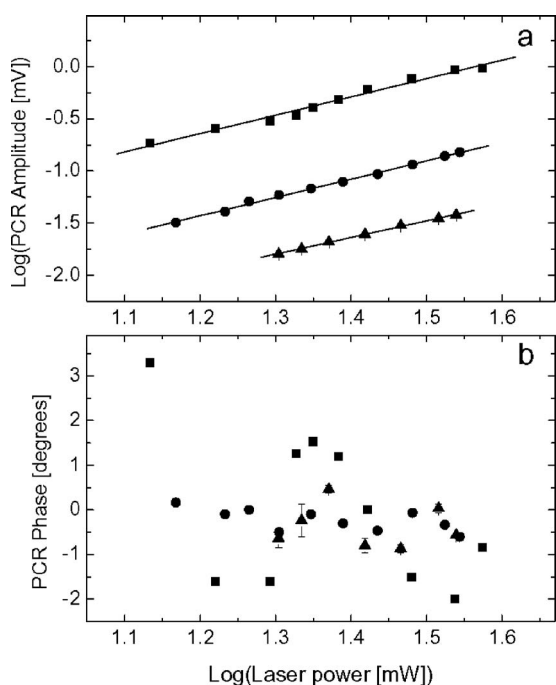


Figure 6. (a) Log-log plot of PCR amplitude and (b) lin-log plot phase vs laser power at 830 nm and 10 kHz from wafer B501 and 24 (■), 387 (●), and 830 μm (▲) spotsizes of the focused laser beam. Slopes of the corresponding best fits (—) for amplitudes: $\beta = 1.76$ (24 μm); 1.76 (387 μm); 1.60 (830 μm).

clear that the values of β decrease with increasing spotsizes, that is, with decreasing laser intensity. Aside from a rigid phase shift associated with the change in the diffusing carrier-wave dimensionality with changing spotsizes shown in Fig. 5b, there is also a dependence of the PCR phase on laser power, indicative of the nonlinear origin of the PCR signal. For fixed spotsizes, the decrease in phase lag is consistent with enhanced carrier-carrier scattering with increasing laser power, leading to accelerated recombination and a decrease in the distance below the wafer surface of the location of the carrier density-wave centroid (the diffusion length, $1/|\sigma_n(\omega)|$, Eq. 2), physically a diffusion-limited free-carrier mean-free path.¹⁵ Decreasing the spotsizes affects the dimensionality of the diffuse carrier wave, enhancing the radial diffusion degrees of freedom and shifting the carrier-wave centroid/phase lag farther away from the surface. The same set of measurements, with the same beam spotsizes, was made with the short lifetime wafer B501 and the results are shown in Fig. 6. The laser power was varied in the range 13.6–37.5 mW and, again, the slopes β were found to decrease with decreasing intensities. Furthermore, they were consistently lower than those measured with the long-lifetime wafer M28. There was no measurable phase shift with laser spotsizes or power changes in Fig. 7. This behavior may be the result of a weaker nonlinearity mechanism in sample B501 than in M28, as expected from the shorter lifetime and smaller photogenerated root-mean-square (rms) free-carrier-density in the former Si wafer.

Another set of measurements was made at 532 nm using the highly focused setup shown in Fig. 4 at 10 kHz. Figure 7a shows the power dependence of PCR amplitude for wafer M28 in the range 6–25 mW. The slope was found to be 1.89. The phase lag exhibited a slight decrease with increasing laser power, Fig. 7b, as expected from enhanced carrier scattering processes. The same measurement was repeated with wafer B501 and the results are shown in Fig. 8. Laser power was varied between 8.7 and 22.4 mW and the amplitude slope was 1.94. No discernible PCR phase dependence on laser power was found. This result at 532 nm is consistent with the 830 nm results obtained with this wafer. They can both be under-

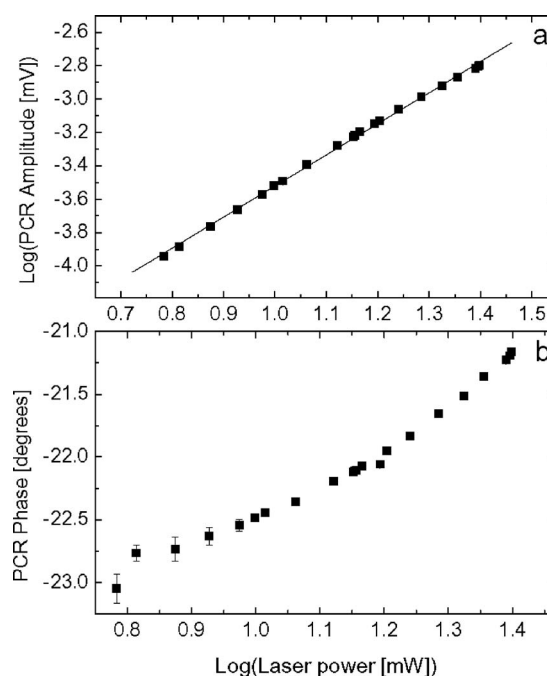


Figure 7. (a) Log-log plot of PCR amplitude and (b) lin-log plot of phase vs laser power (■) at 532 nm and 10 kHz from wafer M28 and 18 μm spotsizes of the focused laser beam. Slope of the corresponding best fit (—) for amplitude: $\beta = 1.89$ (18 μm).

stood in terms of the short recombination lifetime, which renders the subsurface position of the diffusive carrier-wave density centroid¹⁵ essentially independent of lifetime at the frequency of these experiments. The higher slopes than those obtained at 830 nm are due to the increased laser-induced carrier-wave densities as discussed below.

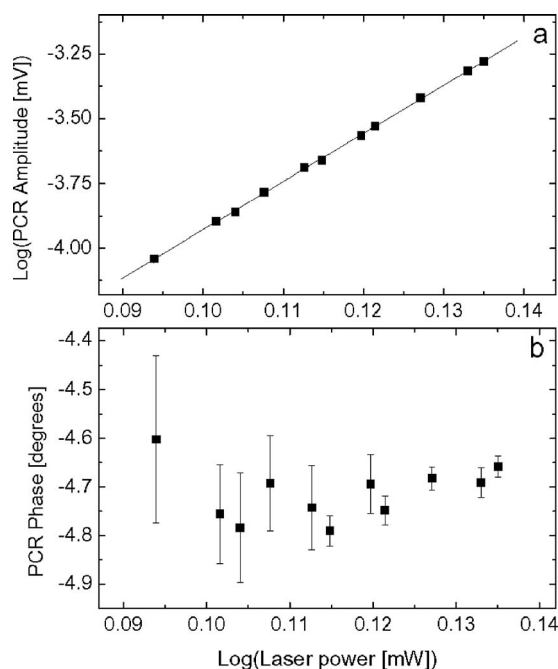


Figure 8. (a) Log-log plot of PCR amplitude and (b) lin-log plot of phase vs laser power (■) at 532 nm and 10 kHz from wafer B501 and 18 μm spotsizes of the focused laser beam. Slope of the corresponding best fit (—) for amplitude: $\beta = 1.94$ (18 μm).

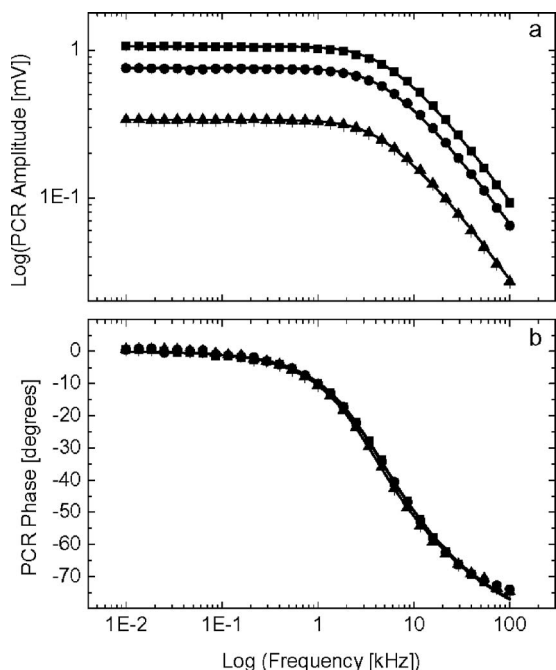


Figure 9. Experimental frequency scans (10 Hz to 100 kHz) of PCR (a) amplitudes and (b) phases from wafer M28 for various 830 nm laser powers focused to an 830 μm spotsize and the corresponding multiparameter theoretical 3D best fit (—) using Eq. 7 with $\beta = 1$. Laser power: 20 (■), 15.2 (●), and 9.6 mW (▲).

Modulation frequency dependence at 830 nm.— Figure 9 shows frequency scans obtained from wafer M28 and three laser powers at a spotsize of 830 nm. The corresponding best fits of the 3D theory, Eq. 15, with $\beta = 1$ to the data are also shown. The phases (Fig. 9b) nearly overlap and thus they appear not to depend strongly on laser power. Figure 5b shows a change of $\sim 10^\circ$ between 1.8 and 15.6 mW at 10 kHz. Small differences on the order of 2° exist among phases across the narrower power range in Fig. 9b; however, they are nearly imperceptible over the full 75° phase range. The frequency dependence of the PCR signals using the same laser powers and 24 and 387 μm spotsizes exhibited similar behavior.

Figure 10 shows the frequency-dependent PCR signals from wafer M28 using 20 mW and various spotsizes, as well as the corresponding best fits to the 3D theory, Eq. 15, with $\beta = 1$. Figure 10b shows significant phase changes with spotsize at high frequencies due to changes in the dimensionality of the PCR signal.¹⁸ The results of best-fitting the 3D theory to the data and extracting transport parameters are shown in Table I. The frequency dependencies of the PCR signals generated with laser powers 15.2 and 9.6 mW and focused on the same spotsizes exhibited similar behaviors.

The theoretical best fits in Fig. 9 and 10 were made using a computational program which minimizes the variance of the combined amplitude and phase fits.¹⁹ Furthermore, the PCR signals were fitted using a nonlinear extension of the foregoing 3D computation algorithm with $\beta = 2$. Fractional powers $1 < \beta < 2$ could not be efficiently accommodated in the 3D PCR theory, Eq. 15. A 1D nonlinear best-fit algorithm was generated based on Eq. 14 and capable of accommodating arbitrary values $1 \leq \beta \leq 2$. The computational algorithm was implemented with the corresponding experimental values for β (Fig. 5 for sample M28) and numerical quantities are presented in Table II. In all tables the photogenerated excess carrier-wave densities (m^{-3}) shown are mean values calculated using the expression

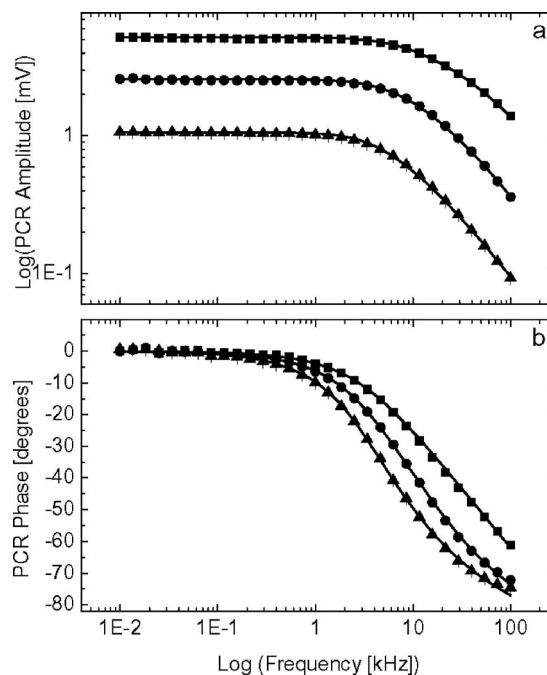


Figure 10. Experimental frequency scans (10 Hz to 100 kHz) of PCR (a) amplitude and (b) phases from wafer M28 for 830 nm and 20 mW laser beam focused to various spotsizes: 24 (■), 387 (●), and 830 μm (▲). Best theoretical 3D fits (—) using Eq. 7 with $\beta = 1$ are also shown.

$$\Delta N = \frac{1}{2} \frac{P_0}{1.6 \times 10^{-19} (\hbar \omega_0)} \left(\frac{\tau}{\pi [W + |L_D(f)|^2 (1/\alpha_p)]} \right) \quad [16]$$

where P_0 is the incident power [W]; $\hbar \omega_0$ is the incident photon energy expressed in eV, where $\omega_0 = hc/\lambda_p$ is the photon angular frequency at the wavelength of the laser; and α_p is the optical absorption coefficient at the excitation wavelength. $L_D(f)$ is the magnitude of the complex carrier diffusion length

$$|L_D(f)| = \frac{\sqrt{D\tau}}{|\sqrt{1 + i2\pi f\tau}|} \quad [17]$$

Values of L_D and τ used in Eq. 14 were calculated from the multiparameter best-fit values obtained from Tables I-IV. From Table I the values of lifetimes obtained with the linear 3D theory, $\beta = 1$, and 24 μm spotsize are reasonable for p-Si,¹⁸ however, the corresponding diffusion coefficients are outside the typical range for p-type wafers.¹⁸ Table I also shows the results of the same experimental data, Fig. 9 and 10, fitted with the 3D theory and $\beta = 2$, Eq. 15. The experimental slope for 24 μm laser spotsize ($\beta = 1.9$) is very close to 2 and validates this fitting procedure. Fitting error was very low, 0.6–0.9%. The measured transport parameters for all laser intensities and 24 μm spotsize can be compared for $\beta = 1$ and 2 from Table I. It is seen that recombination lifetimes consistently decrease in the nonlinear fit. This decrease is larger for higher intensities, reaching up to 43%. The absolute value of the lifetime monotonically decreases with increasing intensity for $\beta = 2$, as expected from the increased carrier-wave densities and the proportionately increased scattering probabilities which limit the diffusion length (or mean free path). In the nonlinear fit, carrier diffusivity values increase dramatically from unrealistically low levels at $\beta = 1$. They rise to values approximately $10 \text{ cm}^2/\text{s}$, which is normal for medium to high injection conditions ($\Delta N \sim 10^{18}$ to 10^{19} cm^{-3}). Front surface recombination velocities also increase considerably in the nonlinear fit and remain essentially unchanged with increasing intensity, as expected, because the defect/recombination center density on the surface is not affected by the incident photon flux. Back

Table I. Best-fitted computational results for sample M28. Experimental data at 830 nm 3D theory and integer values of the nonlinearity coefficient β .

Power P_0 (mW)	Transport and beam parameters	3D model, Eq. 15			
		$\beta = 1$	$\beta = 1$	$\beta = 1$	$\beta = 2$
		24 μm	387 μm	830 μm	24 μm
9.6	I_0 (W/m ²)	21.2×10^2	8.2×10^4	1.8×10^4	21.2×10^6
	ΔN (1/cm ³)	8.0×10^{18}	9.5×10^{16}	3.9×10^{16}	6.6×10^{17}
	τ (μs)	39.3	49.3	84.9	35.9
	D (cm ² /s)	0.31	4.2	9.9	11.1
	S_1 (cm/s)	0.07	980	960	4.3×10^3
	S_2 (cm/s)	2.3×10^4	2.4×10^4	3.7×10^3	1.2×10^4
15.2	I_0 (W/m ²)	33.6×10^6	1.3×10^5	2.8×10^4	33.6×10^6
	ΔN (1/cm ³)	1.5×10^{19}	1.3×10^{17}	4.3×10^{16}	9.6×10^{17}
	τ (μs)	43.5	42.6	55.1	28.8
	D (cm ² /s)	0.26	4.9	5.5	9.9
	S_1 (cm/s)	62	890	787	4×10^3
	S_2 (cm/s)	4.4×10^3	4×10^3	6.8×10^3	1.2×10^4
20	I_0 (W/m ²)	44.2×10^6	1.7×10^5	3.7×10^4	44.2×10^6
	ΔN (1/cm ³)	1.7×10^{19}	1.7×10^{17}	5.4×10^{16}	1.2×10^{18}
	τ (μs)	37.2	43.8	51.6	26.7
	D (cm ² /s)	0.26	5.3	4.7	10
	S_1 (cm/s)	60	890	740	4×10^3
	S_2 (cm/s)	1.7×10^4	6.5×10^3	3.6×10^4	1.2×10^4

surface recombination velocities do not change as dramatically under the nonlinear fit. They are higher than S_1 as expected from the matte nature of the back surfaces of our wafers compared to the polished front surfaces. No attempt for nonlinear fits to the data corresponding to 387 and 830 μm spotsizes was made, as the slopes ($\beta = 1.82$ and 1.72) were far from $\beta = 2$ to guarantee the validity of the 3D computation. As shown in Fig. 2, the best fits of PCR signals

Table II. Best-fitted computational results for sample M28. Experimental data at 830 nm 1D theory and experimental values of nonlinearity coefficient β .

Power P_0 (mW)	Transport and beam parameters	1D model, Eq. 14	
		$\beta = 1.82$	$\beta = 1.72$
		387 μm	830 μm
9.6	I_0 (W/m ²)	8.2×10^4	1.8×10^4
	ΔN (1/cm ³)	4×10^{16}	3.2×10^{16}
	τ (μs)	31.1	81.4
	D (cm ² /s)	25	28.7
	S_1 (cm/s)	1×10^4	7×10^3
	S_2 (cm/s)	420	9.1×10^3
15.2	I_0 (W/m ²)	1.3×10^5	2.8×10^4
	ΔN (1/cm ³)	7.4×10^{16}	4.1×10^{16}
	τ (μs)	27.9	65.8
	D (cm ² /s)	9.2	27.5
	S_1 (cm/s)	4.8×10^4	6.9×10^3
	S_2 (cm/s)	0.3	9.7×10^3
20	I_0 (W/m ²)	1.7×10^5	3.7×10^4
	ΔN (1/cm ³)	8.7×10^{16}	5×10^{16}
	τ (μs)	28	59.8
	D (cm ² /s)	15.3	24.7
	S_1 (cm/s)	1.1×10^4	6.5×10^3
	S_2 (cm/s)	0.2	9.9×10^3

generated with the relatively large spotsizes, $2W \sim 830 \mu\text{m}$, yield similar sets of transport parameters using either 1D or 3D linear theories ($\beta = 1$) only when $\tau < 20 \mu\text{s}$. This is not the case with sample M28 as seen in Table II. However, for comparison with Table II the $\beta = 1$ parameters were calculated using the 3D theory and are shown in Table I. Table II shows results from PCR signals with $2W = 387$ and $830 \mu\text{m}$ fitted to the nonlinear 1D theory, Eq. 14, with $\beta = 1.82$ and 1.72 , from Fig. 5a. In view of Fig. 2 and the best-fitted values of recombination lifetime under all excitation intensities, the calculated transport parameters with the 1D model can only be considered to be approximate. The excess photoinjected carrier densities are somewhat lower than the $2W = 24 \mu\text{m}$ case. Recombination lifetimes under all incident intensities do not change much from the $\beta = 1$ values but they decrease monotonically with increased intensity, as expected for enhanced carrier-carrier scattering.²⁰ The lifetime obtained under 9.6 mW excitation and $2W = 830 \mu\text{m}$ is $81.4 \mu\text{s}$, close to the value $84.9 \mu\text{s}$ obtained from fitting the same data with the 3D theory and $\beta = 1$. These differences increase with increasing incident intensity. As observed with $2W = 24 \mu\text{m}$ spotsize, for nonlinear fits with $\beta = 1.82$ ($2W = 387 \mu\text{m}$) and $\beta = 1.72$ ($2W = 830 \mu\text{m}$) the values of D increased manifold over the $\beta = 1$ values, attaining the normal range of p-Si.¹⁸ However, the values of D are larger than those obtained with $2W = 24 \mu\text{m}$ as expected from the much lower intensities accompanying the larger spotsizes. Only slight decreases are observed with increasing intensity.²⁰ Front and back surface recombination velocities do not undergo significant changes for all nonlinear fits, $\beta = 2$ ($2W = 24 \mu\text{m}$), $\beta = 1.82$ ($2W = 387 \mu\text{m}$), and $\beta = 1.72$ ($2W = 830 \mu\text{m}$). This is as expected from the intrinsic defect structure of the wafer surfaces. S_2 is consistently higher than S_1 for all incident intensities. The comparison between Tables I and II shows that the difference between the $\beta = 1$ values and the nonlinear results is large and due to the nonlinearity exponents $\beta = 1.72$ and 1.82 . This comparison demonstrates the need for precise knowledge of the degree of nonlinearity of the PCR signal in order to obtain physically reasonable and reliable (i.e., self-consistent) measurements of semiconductor transport properties.

Table III. Best-fitted computational results for sample B501. Experimental data at 830 nm with 1D and 3D theories, linear and various nonlinearity coefficients.

Power P_0 (mW)	Transport and beam parameters	3D fitting model		1D fitting model	
		$\beta = 1$		$\beta = 1.76$	$\beta = 1.60$
		387 μm	830 μm	387 μm	830 μm
12	I_0 (W/m ²)	1×10^5	2.2×10^4	1×10^5	2.2×10^4
	ΔN (1/cm ³)	3.6×10^{15}	6.2×10^{14}	1.6×10^{15}	3.9×10^{14}
	τ (μs)	1.3	0.9	0.54	0.55
	D (cm ² /s)	24.6	34.5	23.2	23.4
	S_1 (cm/s)	9.3×10^3	370	390	390
	S_2 (cm/s)	3.9×10^4	2.2×10^4	1.6×10^4	1.6×10^4
38	I_0 (W/m ²)	3.2×10^5	7×10^4	3.2×10^5	7×10^4
	ΔN (1/cm ³)	1×10^{16}	2.2×10^{15}	4.8×10^{15}	1.5×10^{15}
	τ (μs)	1.3	1.1	0.51	0.65
	D (cm ² /s)	32	32.2	23.4	19.5
	S_1 (cm/s)	8×10^3	430	407	920
	S_2 (cm/s)	1.5×10^4	2.4×10^4	1.5×10^4	1.6×10^4

Figure 11 shows two sets of modulation frequency scans obtained from wafer B501, including the corresponding best fits to 3D theory with $\beta = 1$. The phase plots at fixed spotsize nearly overlap, Fig. 11b, and are essentially independent of laser power, consistent with Fig. 6b. Figure 12 shows frequency scans with 38 mW laser power and various spot sizes. The corresponding 3D theoretical best fits to Eq. 15 and $\beta = 1$ are also shown. The phase shifts at the high-frequency end of Fig. 12b are due to changing signal dimensionality from 3D ($2W = 24 \mu\text{m}$) to 1D ($2W = 830 \mu\text{m}$). The frequency dependence of the PCR signals with excitation power 12 mW and the same spot sizes exhibited similar behavior.

The PCR signals of Fig. 11 were fitted to 1D theory using the actual experimental nonlinear values for β , Fig. 6a. Calculated transport parameters are presented in Table III. Unlike sample M28, the short-lifetime ($\tau \sim 1 \mu\text{s}$) wafer B501 did yield PCR frequency scans which could be considered fully one-dimensional under the expanded laser beam spot sizes of 387 and 830 μm , as per the simu-

lations of Fig. 2. At $2W = 24 \mu\text{m}$ the supralinear slope $\beta = 1.76$, Fig. 6a, did not allow use of the 3D Eq. 15 to fit the data and yield representative values of the transport parameters because we could only use integer values of β . Therefore, only fits for the largest two spot sizes are shown in Table III. Here the lifetimes are short for both linear and nonlinear fits and they do not change perceptively with increased laser intensity. This fact may be traced to the relatively low photoexcited carrier-wave densities in the 10^{14} to 10^{15}cm^{-3} range, using Eq. 16 and 17. These are up to four orders of magnitude lower than those estimated for the sample M28. The best-fitted diffusivities are in the range of acceptable values for p-Si¹⁸ and vary little with increased intensity, again due to the relatively low ΔN . Front-surface recombination velocities are lower than back-surface velocities, as expected. There are large differences between the linear and nonlinear fits for the same W which lead to the same conclusion as in the case of wafer M28 in terms of the importance of using the actual nonlinear exponent obtained experimentally in order

Table IV. Best-fitted computational results for sample M28 and B501. Experimental data at 532 nm 3D theory.

Power P_0 (mW)	Transport and beam parameters	3D fitting model for wafer M28		3D fitting model for wafer B501	
		$\beta = 1$	$\beta = 2$	$\beta = 1$	$\beta = 2$
		9.6	I_0 (W/m ²)	3.8×10^7	3.8×10^7
	ΔN (1/cm ³)	3.6×10^{20}	3.1×10^{19}	3×10^{18}	8.3×10^{17}
	τ (μs)	238	70.5	4.2	0.34
	D (cm ² /s)	0.46	2.7	5.7	8.9
	S_1 (cm/s)	123	5.6×10^4	6.7×10^3	3.7×10^3
	S_2 (cm/s)	2×10^4	9.4×10^4	4.2×10^4	9.8×10^3
13.2	I_0 (W/m ²)	5.2×10^7	5.2×10^7	5.2×10^7	5.2×10^7
	ΔN (1/cm ³)	6.1×10^{20}	3.4×10^{19}	4.4×10^{18}	1.2×10^{18}
	τ (μs)	259	56.7	3.5	0.34
	D (cm ² /s)	0.37	2.9	4.7	8.9
	S_1 (cm/s)	184	4.3×10^4	6.3×10^3	3.7×10^3
	S_2 (cm/s)	4.3×10^4	8.6×10^4	3.7×10^4	9.9×10^3
16	I_0 (W/m ²)	6.3×10^7	6.3×10^7	6.3×10^7	6.3×10^7
	ΔN (1/cm ³)	5.9×10^{20}	3×10^{19}	5.5×10^{18}	1.6×10^{18}
	τ (μs)	200	44.5	4.1	0.33
	D (cm ² /s)	0.35	3.2	4.8	6.2
	S_1 (cm/s)	241	4×10^4	7.4×10^3	3.6×10^3
	S_2 (cm/s)	3.9×10^4	6.8×10^4	6.9×10^4	9.6×10^3

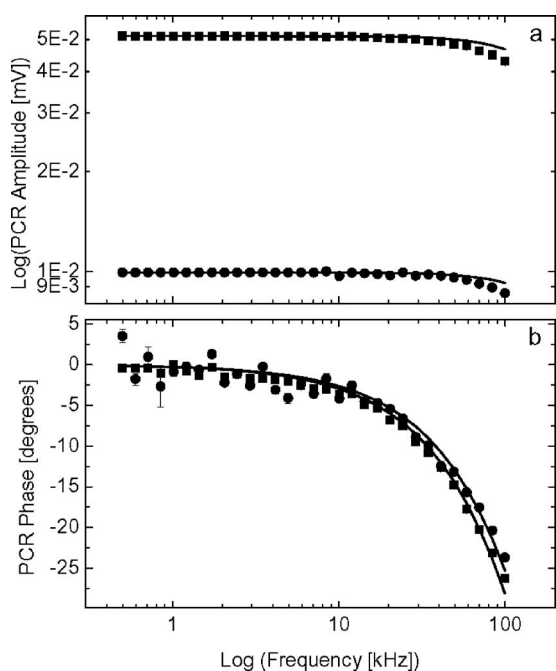


Figure 11. Experimental frequency scans (550 Hz to 100 kHz) of PCR (a) amplitudes and (b) phases from wafer B501 for various 830 nm laser powers focused to an 830 μm spotsize and the corresponding theoretical 3D best fits (—) using Eq. 7 with $\beta = 1$. Laser power: 38 (■) and 12 μm (●).

to calculate the transport parameters. In summary, neither were there large differences in values of the transport parameters between excitation with 12 and 38 mW nor were clear trends in those parameters established. This would be expected under low-injection conditions; however, in these experiments the ΔN range corresponded to intermediate conditions.⁹

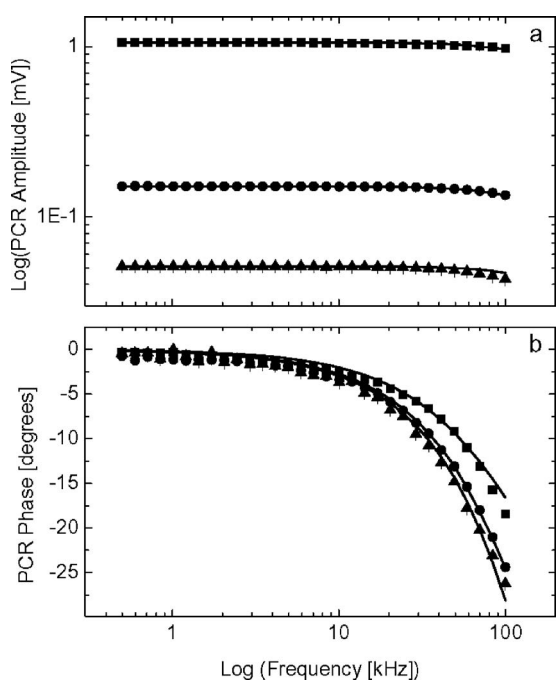


Figure 12. Experimental frequency scans (500 Hz to 100 kHz) of PCR (a) amplitudes and (b) phases from wafer B501 for 830 nm, 38 mW laser beam focused to various spot sizes: 24 (■), 387 (●), and 830 μm (▲). Best theoretical 3D (—) using Eq. 7 with $\beta = 1$ are also shown.

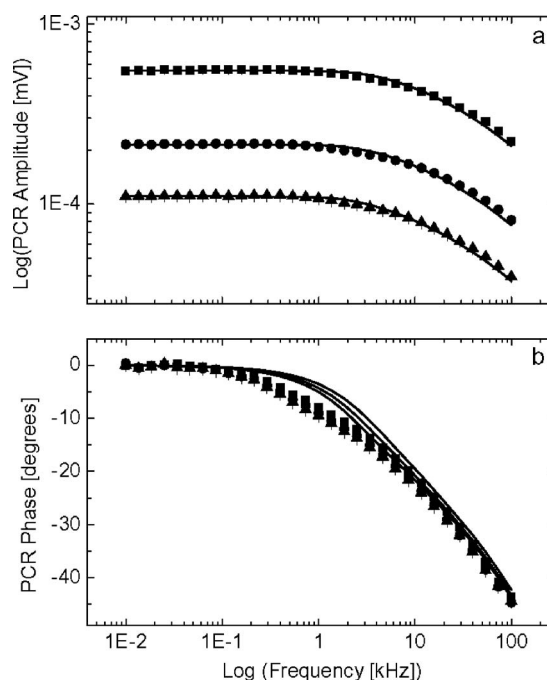


Figure 13. Experimental frequency scans (10 Hz to 100 kHz) of PCR (a) amplitudes and (b) phases from wafer M28 for various 532 nm laser powers focused to an 18 μm spotsize and the corresponding theoretical 3D best fits (—) using Eq. 7 with $\beta = 2$. Laser power: 16 (■), 13.2 (●), and 9.6 mW (▲).

Modulation frequency dependence at 532 nm.— Figures 13 and 14 show the frequency dependent amplitude and phase of the PCR signal from wafers M28 and B501, respectively, using several laser powers and 18 μm spotsize. The corresponding best fits to the 3D

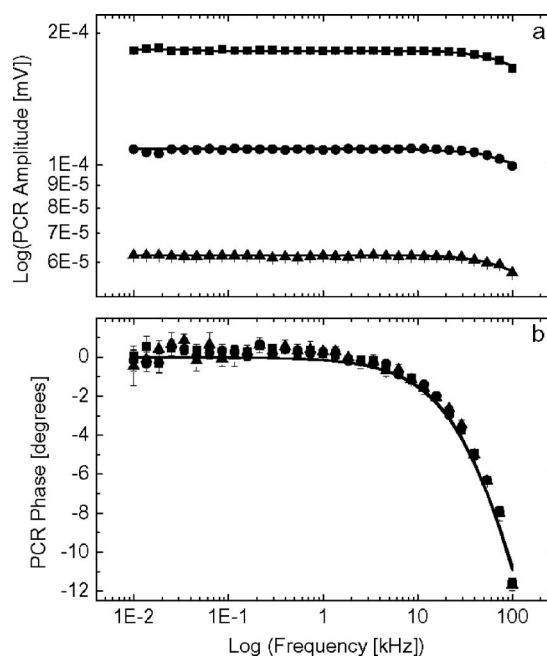


Figure 14. Experimental frequency scans (10 Hz to 100 kHz) of PCR (a) amplitudes and (b) phases from wafer B501 for various 532 nm laser powers focused to an 18 μm spotsize and the corresponding theoretical 3D best fits (—) using Eq. 7 with $\beta = 2$. Laser power: 16 (■), 13.2 (●), and 9.6 mW (▲).

theory, Eq. 15, are also shown. While the amplitudes scale nonlinearly with laser power with slopes $\beta = 1.89$ (M28, Fig. 7a) and $\beta = 1.94$ (B501, Fig. 8a), the phases at the various laser powers nearly overlap, consistent with Fig. 7b and 8b. The best fits to Eq. 15 presented in Fig. 13a and 14a were made using $\beta = 2$. This value of β is close to the experimentally measured slopes; therefore, it is expected that transport parameters obtained from these fits are close to those that would have been obtained using the exact experimental supralinear slopes. The multiparameter best-fit results to the data are presented in Table IV for three laser powers. For sample M28 the values of τ decrease with increasing laser intensity, in a manner similar to that observed with 830 nm irradiation, Table I. The relative values of τ for excitation with beam spot sizes 18 and 24 μm at the two distinct wavelengths, Tables I and IV, are quite close, within a factor of two. In Table IV the values of τ obtained with $\beta = 2$ for the three incident intensities I_0 are more than three times smaller than those obtained with $\beta = 1$. Once again, this shows the dramatic difference the nonlinearity coefficient value can make in PCR measurements. The diffusion coefficients obtained using $\beta = 1$ are far from the range of acceptable values for this parameter for p-type wafers,¹⁸ and those obtained with $\beta = 2$ are marginally within the range of typical values. This is approximately 1 order of magnitude smaller than the D values obtained in Table I and is probably due to the much stronger carrier-carrier scattering at high-injection carrier-wave densities in the 10^{19} to 10^{20} cm^{-3} range.²⁰ The best-fitted values of S_1 obtained with $\beta = 1$ are more than 100 times lower than those obtained with $\beta = 2$. The latter values are essentially independent of laser intensity (also the case in Table I under 830 nm excitation) but are clearly higher than their $\beta = 2$ counterparts in Table I. This, along with differences in τ (523 nm) and τ (830 nm), is expected, because the optical absorption depth at 523 nm is much shorter (0.96 μm ; $\alpha_p = 10,340$ cm^{-1}) than that at 830 nm (15.2 μm ; $\alpha_p = 658.9$ cm^{-1}), with the consequence that optical injection samples the defect densities in the near-surface region much more strongly at 523 nm than at 830 nm thus exhibiting enhanced sensitivity to surface recombination and yielding a larger effective surface recombination velocity S_1 . The back-surface recombination velocities are all in the range of 10^4 cm/s for both wavelengths, Tables I and IV. Physically, they should be the same; however, our simulations show that the shallower optical penetration depth at 523 nm renders the PCR signal less sensitive to S_2 than that at 830 nm. Therefore, the discrepancy is probably due to increased tolerance for a wider range of best-fitted S_2 values of the computational algorithm.

The best fits to Eq. 15 resulting from the B501-sample experimental data with $\beta = 1$ and 2 are also shown in Table IV. The values of τ obtained with $\beta = 2$ which are close to the experimental value $\beta = 1.94$ for all laser powers are in the sub- μs range, consistent with those obtained at 830 nm in Table III. In fact, they are approximately two times smaller under 523 nm excitation than expected from a significantly higher intensity range (about 3 orders of magnitude) and the corresponding high-injection ramifications. The τ values obtained with the linear fit are unrealistic in comparison with other data in Table III, more than ten times larger than those obtained with $\beta = 2$. The carrier diffusivity values in Table IV are considerably smaller than those in Table III and decrease with increased power from 9.6 to 16 mW. These trends are consistent with the shallower penetration depth, higher photoinjected carrier-wave densities, and higher laser intensities under 523 nm excitation.²⁰ In a manner similar to the behavior of sample M28, the S_1 values under 523 nm excitation are higher than under 830 nm, whereas values of S_2 are close. Overall, values of the transport parameters in Table IV fitted with $\beta = 1$ show some significant deviations from the nonlinear fits, especially for τ and S_1 .

For both samples, the three-orders-of-magnitude higher intensities and shorter optical absorption depth at 523 nm are associated with increased nonlinearity exponents which tend to values closer to 2, a limiting value for electron-hole band-to-band bipolar

recombination.^{5,7,8} In that limit, band-to-defect recombination may be dominated by the $N \times P$ product of electron-hole density recombination, and a different mechanism for quadratic PL dependence on photocarrier density may have to be considered, as proposed by Guidotti et al.⁵ and Nuban et al.^{7,8} and discussed in the context of Eq. 1.

Nonlinearity Ratios

The structure of the Drude equation, Eq. 5, which leads to the dependence of the PCR signal on supralinear integrals of ΔN^β , Eq. 12 and 13, implies the existence of higher harmonics under harmonic excitation. Specifically, we can define a carrier-density dependent quantity

$$J(\omega; \beta) \equiv \left[N_0 + \frac{1}{2} \Delta N (1 + e^{i\omega t}) \right]^\beta \quad [18]$$

where N_0 is the residual equilibrium carrier concentration and ΔN is the excess photocarrier density. Equation 18 can be conveniently rearranged in two limiting cases.

Low-injection limit, $\Delta N/2N_0 < 1$.—Equation 18 can be expanded by use of the binomial theorem

$$J(\omega; \beta) = N_0^\beta \left[1 + \beta \left(\frac{\Delta N}{2N_0} \right) \times (1 + e^{i\omega t}) + \frac{\beta(\beta-1)}{2!} \left(\frac{\Delta N}{2N_0} \right)^2 (1 + e^{i\omega t})^2 + \dots \right] \quad [19]$$

$\beta - n \geq 0$

For $\beta \leq 2$ as is the case in our experiments, we find

$$J(\omega; \beta) = N_0^\beta [F_0 + F_1 e^{i\omega t} + F_2 e^{2i\omega t}] \quad [20]$$

where

$$F_0 \equiv 1 + \beta \left(\frac{\Delta N}{2N_0} \right) + \frac{\beta(\beta-1)}{2!} \left(\frac{\Delta N}{2N_0} \right)^2$$

$$F_1 \equiv \beta \left(\frac{\Delta N}{2N_0} \right) + \frac{2\beta(\beta-1)}{2!} \left(\frac{\Delta N}{2N_0} \right)^2$$

$$F_2 \equiv \frac{\beta(\beta-1)}{2!} \left(\frac{\Delta N}{2N_0} \right)^2 \quad [21]$$

The amplitude of the ratio F_2/F_1 is, to leading order in $\Delta N/N_0$ under low-injection conditions

$$\left| \frac{F_2(2\omega)}{F_1(\omega)} \right| \approx \frac{\beta-1}{2} \left(\frac{\Delta N}{N_0} \right) \propto I_0 \quad [22]$$

Therefore, under low-injection conditions the theory predicts a linear dependence of the ratio of the second harmonic to the fundamental component of the PCR signal amplitude on the incident laser intensity. Assuming a complex free-carrier-wave density $\Delta N(\omega) = |\Delta N(\omega)|e^{i\phi}$, Eq. 22 also predicts a phase difference between F_1 and F_2 which is independent of I_0 .

High-injection limit, $\Delta N/2N_0 > 1$.—Equation 18 can be rewritten and expanded by use of the binomial theorem

$$J(\omega; \beta) = \left(\frac{\Delta N}{2} \right)^\beta \left[(1 + e^{i\omega t})^\beta + \beta \left(\frac{2N_0}{\Delta N} \right) (1 + e^{i\omega t})^{\beta-1} + \frac{\beta(\beta-1)}{2} \left(\frac{2N_0}{\Delta N} \right)^2 (1 + e^{i\omega t})^{\beta-2} + \dots \right] \quad [23]$$

If $\beta \leq 2$, then

$$J(\omega; \beta) = \left(\frac{\Delta N}{2} \right)^\beta [G_0 + G_1 e^{i\omega t} + G_2 e^{2i\omega t}] \quad [24]$$

where

$$G_0 = 1 + \beta \left(\frac{2N_0}{\Delta N} \right) + \frac{\beta(\beta-1)}{2!} \left(\frac{2N_0}{\Delta N} \right)^2$$

$$G_1 = \beta + \beta(\beta-1) \left(\frac{2N_0}{\Delta N} \right)$$

$$G_2 = \frac{\beta(\beta-1)}{2!} \quad [25]$$

The amplitude of the ratio G_2/G_1 is, to leading order in $N_0/\Delta N$ under high-injection conditions

$$\left| \frac{G_2(2\omega)}{G_1(\omega)} \right| \approx \frac{\beta(\beta-1)}{2!\beta} = \frac{1}{2}(\beta-1) = 0.5 \text{ if } \beta \approx 2 \quad [26]$$

Assuming $\Delta N(\omega) = |\Delta N(\omega)|e^{i\phi}$, and retaining the second term in G_1 , Eq. 25, we obtain from Eq. 24

$$R_{21} \equiv \frac{G_2(2\omega)}{G_1(\omega)} = \frac{1}{2 + \left(\frac{4N_0}{|\Delta N|} \right) e^{-i\phi}} \equiv |R_{21}|e^{i\phi_R} \quad [27]$$

where $|R_{21}| \approx 1/2$ as for the case $2N_0 \ll |\Delta N|$, and

$$\Phi_R = -\tan^{-1} \left[\frac{\rho \sin \phi}{I_0 + \rho \cos \phi} \right] \quad [28]$$

Here $\Delta N = I_0 \Delta n$ emphasizes the linear dependence of ΔN on incident laser intensity; ρ is defined as $\rho \equiv 2N_0/|\Delta n|$. Equations 26 and 28 show that under high-injection conditions the ratio of the second harmonic to the fundamental has an amplitude of approximately 0.5 for nonlinearity coefficients β close to 2; the phase difference $\Phi_R(I_0)$ decreases as I_0 increases. This can be easily seen if the tangent is written in terms of its constituent sine and cosine

$$\sin \Phi_R = \frac{\rho \sin \phi}{\sqrt{(I_0 + \rho \cos \phi)^2 + \rho^2 \sin^2 \phi}}$$

$$\cos \Phi_R = \frac{I_0 + \rho \sin \phi}{\sqrt{(I_0 + \rho \cos \phi)^2 + \rho^2 \sin^2 \phi}} \quad [29]$$

When I_0 increases, $\sin[\Phi_R(I_0)]$ decreases and $\cos[\Phi_R(I_0)]$ increases, i.e., Φ_R decreases. These trends in amplitude and phase of the second harmonic to fundamental PCR signal components can be readily tested experimentally from the respective 1f and 2f channels of the lock-in amplifier. The results for sample M28, which exhibits a stronger nonlinearity than B501 due to the larger photocarrier-wave densities, are shown in Fig. 15. It is clearly seen that the ratio of amplitudes is approximately equal to 0.5 across the entire power/intensity range of the incident laser light at 523 nm and 18 μm spotsize. The phase difference is also a monotonically decreasing function of I_0 . We were not able to obtain a 2f contribution from sample B501 because the signal was too low and the noise significant. In conclusion, the nonlinearity ratio test can be used to clarify the injection levels of particular experimental conditions. In our experiments, the test has shown conclusively that we were operating under high-injection conditions.

Conclusions

Theoretical nonlinear PCR studies and experiments with Si wafers have been performed to investigate the dependence of the signal on the exciting superbandgap laser beam power P_0 or intensity I_0 . Of central importance to this work was a study of any differences between derived values of the electronic transport parameters of silicon wafers when theoretical diffusion-wave models take into account the experimentally measured nonlinearity coefficient β and those values derived on the usual assumption of linear dependence of the PCR signal on I_0 ($\beta = 1$). The appearance of nonlinearity in the free-carrier transport equations was attributed, in a first instance, to the dependence of the electronic relaxation time, τ_s , on excess

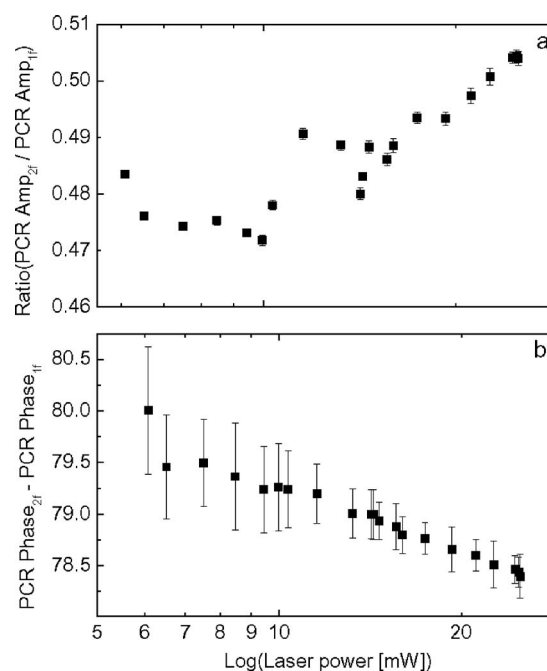


Figure 15. (a) Lin-log plots of the relation between first and second harmonic of PCR amplitudes and (b) difference between first and second harmonic of PCR phases vs laser power (■) at 532 nm and 10 kHz from wafer M28 and 18 μm spotsize of the focused laser beam.

free-carrier density, Δn , which affects the overall Δn power dependence of the infrared free-carrier absorption coefficient via the Drude formula. Transport properties were derived through fitting the experimental PCR frequency scans (amplitudes and phases) to linear and nonlinear theoretical diffuse carrier-wave density models in one and three dimensions via a multiparameter fitting computational procedure. Special attention was paid to the influence of laser parameters, such as wavelength, beam spotsize, and power/intensity, on the semiconductor transport properties. Large discrepancies in the four transport parameters (recombination lifetime, carrier diffusivity, and front- and back-surface recombination velocities) were found between the linear and nonlinear approaches for two silicon samples with long and short recombination lifetimes. Using the fundamental and second harmonic amplitudes and phases under harmonic optical excitation, the nonlinear dependence of the PCR signals on laser power was found to be consistent with high optical injection of free-carriers in the semiconductor. It was also shown that the value of β can be determined by the second harmonic-to-fundamental-amplitude ratio and is controlled by the carrier relaxation time dependence on the optically injected excess diffusive photocarrier density wave.

Acknowledgments

The financial support of the Ontario Centers of Excellence (OCE) through a Collaborative Contract and of the Natural Sciences and Engineering Council of Canada (NSERC) for a Discovery Grant to A.M. are gratefully acknowledged. A.M. wishes to thank the Alexander von Humboldt Foundation for a Research Award which partially supported M.P.'s research leave at the University of Toronto. This work was partially performed within the framework of GRK384.

Appendix A

Symbol Definitions Appearing in Eq. 8 and 15

$$\Delta \tilde{N}(q; \omega) = \int_0^L \tilde{N}(q, z; \omega) dz = E_{3D}(q, \omega) M_{3D}(q, \omega) \quad [A-1]$$

$$E_{3D}(q, \omega) = \frac{\alpha_P I_0 \eta_n (1-R) e^{-\frac{q^2 W^2}{4}}}{2h\nu D [\alpha_P^2 - \xi_c^2]} \quad [\text{A-2}]$$

$$M_{3D}(q, \omega) = \frac{(1 - e^{-\xi_c L})}{\xi_c} [C_1(q, \omega) + C_2(q, \omega) e^{-\xi_c L}] - \frac{(1 - e^{-\alpha_P L})}{\alpha_P} \quad [\text{A-3}]$$

$$\xi_c^2 = q^2 + \sigma_c^2 \quad [\text{A-4}]$$

$$\sigma_c^2 = \frac{1 + i\omega\tau}{D\tau} \quad [\text{A-5}]$$

$$C_1(q, \omega) = A_1 A_2 \left[\frac{b_1 - b_2 e^{-(\alpha_P - \xi_c)L}}{A_2 - A_1 e^{-2\xi_c L}} \right] \quad [\text{A-6}]$$

$$C_2(q, \omega) = \frac{b_1 A_1 - b_2 A_2 e^{-(\alpha_P - \xi_c)L}}{A_2 - A_1 e^{-2\xi_c L}} \quad [\text{A-7}]$$

$$A_1 = \frac{D\xi_c - S_1}{D\xi_c + S_1} \quad [\text{A-8}]$$

$$A_2 = \frac{D\xi_c + S_2}{D\xi_c - S_2} \quad [\text{A-9}]$$

$$b_1 = \frac{D\alpha_P + S_1}{D\xi_c - S_1} \quad [\text{A-10}]$$

$$b_2 = \frac{D\alpha_P - S_2}{D\xi_c + S_2} \quad [\text{A-11}]$$

In the foregoing expressions, α_P and P_0 are the absorption coefficient of the semiconductor at the excitation (pump) wavelength and the power of the superbandgap excitation laser, respectively; η_n is the optical-to-electronic energy conversion efficiency; R is the reflectivity of the wafer surface on which the laser beam impinges. D and τ are the carrier diffusion coefficient and effective recombination lifetime, respectively. W is the $(1/e^2)$ -radius of the Gaussian excitation beam (or laser beam spotsize). S_1 and S_2 are the front and rear surface recombination velocities of the sample, respectively.

Appendix B

Symbol Definitions Appearing in Eq. 9 and 14

$$S_{1D}(\omega) = C \int_0^L \Delta N(z; \omega) dz = CE_{1D}(\omega) M_{1D}(\omega) \quad [\text{B-1}]$$

$$E_{1D}(\omega) = \frac{I_0 \eta_n \alpha_P (1-R)}{2h\nu D [\alpha_P^2 - \sigma_c^2]} \quad [\text{B-2}]$$

$$M_{1D}(\omega) = \frac{\gamma_1 (\Gamma_2 + e^{-\sigma_c L}) - \gamma_2 (\Gamma_1 e^{-(\alpha_P + \sigma_c)L} + e^{-\alpha_P L})}{\Gamma_2 - \Gamma_1 e^{-2\sigma_c L}} - \frac{\sigma_c}{\alpha_P} (1 - e^{-\alpha_P L}) \quad [\text{B-3}]$$

$$\sigma_c = \sqrt{\frac{1 + i\omega\tau}{D\tau}} \quad [\text{B-4}]$$

$$\Gamma_1 = \frac{D\sigma_c - S_1}{D\sigma_c + S_1} \quad [\text{B-5}]$$

$$\Gamma_2 = \frac{D\sigma_c + S_2}{D\sigma_c - S_2} \quad [\text{B-6}]$$

$$\gamma_1 = \frac{D\alpha_P + S_1}{D\sigma_c - S_1} \quad [\text{B-7}]$$

$$\gamma_2 = \frac{D\alpha_P - S_2}{D\sigma_c + S_2} \quad [\text{B-8}]$$

The definitions of the symbols are the same as in Appendix A.

References

1. D. K. Schroder, *Semiconductor Material and Device Characterization*, 2nd ed., p. 427, Wiley, New York (1998).
2. A. Mandelis, J. Batista, and D. Shaughnessy, *Phys. Rev. B*, **67**, 205208 (2003).
3. J. Batista, D. Shaughnessy, and A. Mandelis, *J. Appl. Phys.*, **97**, 023701 (2005).
4. A. Mandelis, *J. Appl. Phys.*, **97**, 083508 (2005); A. Mandelis, J. Batista, J. Gibkes, M. Pawlak, and J. Pelzl, *J. Appl. Phys.*, **97**, 083507 (2005).
5. D. Guidotti, J. S. Batchelder, A. Finkel, and J. A. Van Vechten, *Phys. Rev. B*, **38**, 1569 (1988); D. Guidotti, J. S. Batchelder, A. Finkel, P. D. Gerber, and J. A. Van Vechten, *J. Appl. Phys.*, **66**, 2542 (1989).
6. J. R. Haynes and C. W. Westphal, *Phys. Rev.*, **86**, 647 (1956).
7. S. K. Krawczyk and M. F. Nuban, *Mater. Sci. Eng., B*, **28**, 452 (1994).
8. M. F. Nuban, S. K. Krawczyk, and N. Bejar, *Mater. Sci. Eng., B*, **44**, 125 (1997).
9. W. M. Bullis and H. R. Huff, *J. Electrochem. Soc.*, **143**, 13399 (1996).
10. F. K. Reinhart, *J. Appl. Phys.*, **99**, 073102 (2006).
11. M. A. Weinstein, *Am. J. Phys.*, **28**, 123 (1960); A. Bauer, *Optik (Stuttgart)*, **29**, 179 (1969).
12. K. Seeger, *Semiconductor Physics, Springer Series on Solid State Science*, Vol. 40, Springer-Verlag, New York (1982).
13. M. Miyao, T. Motooka, N. Natsuaki, and T. Tokuyama, *Solid State Commun.*, **37**, 605 (1981).
14. T. Ikari, A. Salnick, and A. Mandelis, *J. Appl. Phys.*, **85**, 7392 (1999).
15. A. Mandelis, *Diffusion-Wave Fields: Mathematical Methods and Green Functions*, Chap. 9, Springer, New York (2001).
16. T. Seidel, *Metallurgy of Elemental and Compound Semiconductors*, R. O. Grubel, Editor, Interscience, New York (1961).
17. *Handbook of Optical Constants of Solids III*, E. D. Palik, Editor, p. 529, Academic, New York (1998).
18. M. E. Rodriguez, A. Mandelis, G. Pan, L. Nicolaides, J. A. Garcia, and Y. Riopel, *J. Electrochem. Soc.*, **147**, 687 (2000).
19. B. Li, D. Shaughnessy, and A. Mandelis, *J. Appl. Phys.*, **97**, 023701 (2005).
20. C. M. Li, T. Sjudin, and H. L. Dai, *Phys. Rev. B*, **56**, 15252 (1997).